ADVANCED FUNCTIONAL MATERIALS
www.afm-journal.de

Direct Transcription of Two-Dimensional Colloidal Crystal Arrays into Three-Dimensional Photonic Crystals

Alexandru Vlad, Andreas Frölich,* Thomas Zebrowski, Constantin Augustin Dutu, Kurt Busch, Sorin Melinte, Martin Wegener, and Isabelle Huynen*

A simple protocol for the fabrication of three-dimensional (3D) photonic crystals in silicon is presented. Surface structuring by nanosphere lithography is merged with a novel silicon etching method to fabricate ordered 3D architectures. The SPRIE method, sequential passivation reactive ion etching, is a one-step processing protocol relying on sequential passivation and reactive ion etching reactions using C_4F_8 and SF_6 plasma chemistries. The diffusion of fresh reactants and etch product species inside the etched channels is found to play an important role affecting the structural uniformity of the designed structures and the etch rate drift is corrected by adjusting the reaction times. High quality photonic crystals are thus obtained by adding the third dimension to the two-dimensional (2D) colloidal crystal assemblies through SPRIE. Careful adjustments of both mask design and lateral etch extent balance allow the implementation of even more complex functionalities including photonic crystal slabs and precise defect engineering. 3D photonic crystal lattices exhibiting optical stop-bands in the infrared spectral region are demonstrated, proving the potential of SPRIE for fast, simple, and large-scale fabrication of photonic structures.

1. Introduction

Next generation nanoscale device fabrication and commercialization will rely on simple and low-cost large-area nanofabrication approaches and subsequent lining with the macroscopic world. Present established technologies are either time consuming, limited to research and development applications mainly in small batch production (for example, electron-beam lithography, printing or scanning probe techniques) or highly sophisticated and costly, requiring extensive maintenance and not being readily accessible (such as X-ray, extreme UV or projection lithography techniques). Self-assembly is believed to be a key technology for next generation surface and volume nanostructuring applications.[1–4] Feature-size control down to the molecular level and easy synthesis together with a large versatility in the physicochemistry of the respective materials are the main reasons behind the tremendous work devoted to self-assembled systems. Electronics, photonics, energy storage, materials science, chemical industry and biotechnology already show great improvements following the introduction of the zeolites, mesoporous materials, nanostructured block copolymers, inorganic oxides, and track etched membranes as well as of colloidal micro- and nanoassemblies into their processing core.[5,6]

Photonic technology can overcome some major hurdles related to the electronic industry especially when dealing with speed and bandwidth limitations.[7] Optical data recording and transfer or laser technology are successfully implemented applications. When it comes to on-chip photon routing, photonic crystals remain the best candidates due to low losses, inherent

Dr. A. Vlad, C. A. Dutu, Prof. S. Melinte, Prof. I. Huynen
Institute of Information and Communication Technologies
Electronics and Applied Mathematics
Electrical Engineering
Université catholique de Louvain
1348 Louvain la Neuve, Belgium
E-mail: alexandru.vlad@uclouvain.be

A. Frölich, Prof. M. Wegener
Institut für Angewandte Physik
Karlsruhe Institute of Technology (KIT)
Wolfgang-Gaede-Straße 1, 76131 Karlsruhe, Germany
E-mail: andreas.froelich@kit.edu

A. Frölich, T. Zebrowski, Prof. M. Wegener
DFG-Center for Functional Nanostructures (CFN)
Karlsruhe Institute of Technology (KIT)
Wolfgang-Gaede-Straße 1, 76131 Karlsruhe, Germany

T. Zebrowski
Institut für Theoretische Festkörperphysik
Karlsruhe Institute of Technology (KIT)
Wolfgang-Gaede-Straße 1, 76131 Karlsruhe, Germany

Prof. K. Busch
Humboldt Universität zu Berlin
AG Theoretische Optik & Photonik
Newtonstraße 15, 12489 Berlin
Germany and Max Born Institut
Max-Born-Straße 2A, 12489 Berlin, Germany

DOI: 10.1002/adfm.201201138

to their dielectric nature, as compared to plasmonic devices, promising further reduction of the footprint area of all-optical devices.[8] Amongst the photonic crystals architectures, the 3D design remains the most challenging in fabrication and implementation. This originates from the stringent constitutional, quality and functional requirements. Structuring dielectric materials at the 100-nm scale and with 3D periodicity is not straightforward and several methods have been proposed to address this bottleneck. Artificial opals and their inverted replicas are the most studied examples given the simplicity in fabrication and relatively good optical performances.[1,9–11] Recent developments have further enhanced their complexity by using non-spherical particles[12,13] or binary colloidal dispersions[3] and controllable realization of 3D defects.[14,15] Simultaneously, surface micromachining allowed the realization of photonic crystals with symmetries other than f.c.c. and defect engineering controlled to a great extent.[16] However, this approach is costly and time consuming because it is based on consecutive, layer-by-layer, nanostructuring and planarization steps.

Alternatively, direct writing or single-step processing techniques have emerged as powerful tools for rapid and scalable fabrication of 3D photonic crystals. The multiphoton polymerization lithography seems an attractive scenario as it allows for an unprecedented control of the crystal geometry and controlled defect incorporation, although it suffers from low throughput due to the serial writing procedure.[17,18] Interference, holographic, or phase-shift lithography provide a higher throughput, yet have limited design flexibility.[19–21] Recently, electron beam lithography combined with stacked resist compositions and modulated exposure profiles enabled direct writing of 3D lattices with periodicities and feature-sizes suitable for visible-spectrum photonic crystals.[22] Nevertheless, all these techniques rely on the use of photo- or electron-sensitive polymers so the fabricated structures have a low index contrast to air. Through inversion or by using chalcogenide glasses a higher index contrast can be obtained however, requiring additional processing steps and hence, unavoidable fabrication defects.[23,24] Direct writing of large-area 3D photonic lattices in high refractive index materials (like silicon) has been realized by modulated electrochemical etching[25] or by angled dry etching.[26,27] The limitations are the limited resolution (close to one micrometer, intrinsic to the electrochemical procedure) for the former and the use of relatively complex procedures for masking, alignment and processing for the latter.

Spherical colloidal micro- and nanoparticles made of dielectric materials have been extensively used in the field of nanophotonics given their specific size close to the characteristic dimensions required for an efficient light–matter interaction.[1,9,28–30] The fabrication of 2D and 3D photonic crystal structures and the realization of various plasmonic platforms for biosensing, surface enhanced Raman spectroscopy or metamaterial applications over large areas are easy tasks using the respective colloids.[2,31,32] Though there are some intrinsic disadvantages, mainly related to the available shapes and self-assembled geometries, recent developments have shown that these limitations can be defeated through rational design and precise engineering of the component particles and assembly techniques. Depending on the initial configuration of the colloidal crystals several approaches have been developed. For example, the 3D colloidal templates (usually in the opal-like form) are either used as such or inverted to generate replica templates made of a desired material and explored, due to their intrinsic volume structuring, as platforms for 3D photonic applications. In turn, the 2D assemblies have been mainly used for surface structuring with few attempts on volume structuring.[28]

Here, we report on a large area 3D structuring strategy for advanced photonic materials by adding the third dimension to 2D etch masks. The 2D masks are obtained via nanosphere lithography (NSL), whereas sequential passivation reactive ion etching (SPRIE) is used to add the third dimension. Instead of generating smooth and straight etch profiles we have adapted the procedure in such a way that it produces regular size variations in the etch profile. The fabricated structures display photonic stop-bands proving the suitability of the method for the realization of 3D photonic crystals. Moreover, the highly engineered materials are generated in a single-step 3D structuring protocol providing an alternative to the developed techniques for direct writing of photonic lattices. Though the method was originally proposed by Prather et al., their study was limited to theoretical analysis and microfabrication realization possibilities without a complete implementation of photonic crystals.[33]

2. Results and Discussion

2.1. From DRIE to SPRIE

The deep reactive ion etching (DRIE) method itself is not new and has been used extensively for silicon micromachining. The method was invented by Laemer and Schilp and is also known as time-multiplexed alternating process or, more commonly, as the Bosch method.[34] It has been developed and extensively used for the high-aspect ratio micro- and nanostructuring of silicon for various applications, including microfluidics, actuation and optics. The huge interest in DRIE was triggered by several advantages provided over other silicon etching techniques: very high aspect ratios, etch selectivity and a relatively simple experimental configuration. Technical details and an exhaustive description of the etch mechanism and developed recipes can be found in the literature; here only a schematic representation of the method is presented to provide a better understanding of the developed protocol.[35] The principle behind the classical DRIE protocol is depicted in **Figure 1**a. There are two distinct steps involved in the process: i) silicon etching and ii) side-wall passivation. The chemistries are different and most commonly based on SF_6 and C_4F_8 reactive plasmas. While the former is used to isotropically etch the silicon, the latter produces a thin fluoropolymer conformal coating protecting the etched part from the subsequent corrosion through the following simplified reactions:[35]

$$\begin{aligned} &\text{etch}: SF_6 + e^- \rightarrow SF_5^+ + F\bullet + 2e^-; \\ &Si_{(solid)} + 4F\bullet_{(gas)} \rightarrow SiF_{4(gas)} \end{aligned} \quad (1)$$

$$\begin{aligned} &\text{passivation}: C_4F_8 + e^- \rightarrow C_3F_6 + CF_2 + e^-; \\ &n\bullet\bullet\ CF_{2\,(gas)} \rightarrow (CF_2)_{n(solid)} \end{aligned} \quad (2)$$

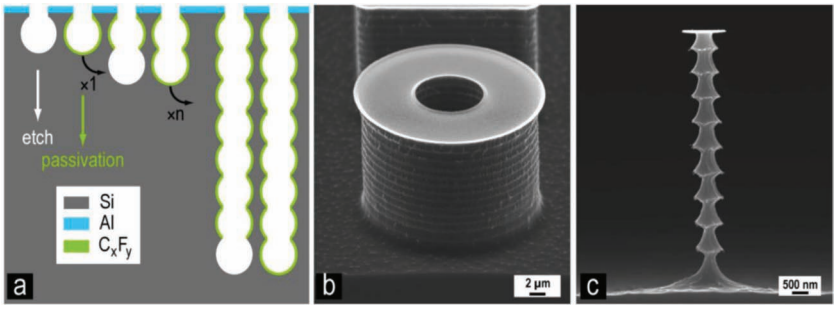

Figure 1. Process overview. a) Schematic diagram of the DRIE or SPRIE process. b) Typical silicon DRIE profile showing relatively smooth and straight Si sidewalls. c) Diameter modulated silicon nanopillar generated using SPRIE.

The actual chemistry is, however, more complicated during real processing as mixing of the process gases occurs and there is no longer a clear distinction between etch and passivation steps. This is due to the limited diffusion of reactive species and released products given the short reaction times that are typically used (of the order of few seconds). Hence, by carefully adjusting this balance, straight and deep etch profiles are obtained (Figure 1b). This configuration is highly desirable for silicon micromachining technology and much effort has been put into optimizing and controlling the aspect ratio, taper angle and minimizing the scalloping (i.e., the generation of side protrusions). Intriguingly, the scalloping effect can also be harnessed for 3D micro- and nanostructuring. For instance, by rigorously decoupling each passivation/etch iteration, for example by including a pump–purge step, pronounced in-plane protrusions are obtained leading to a large variety of 3D nanostructures depending on the configuration of the etch mask. An example of a diameter modulated silicon nanopillar is shown in Figure 1c. In the following we will show how the combination of 2D ordered masks with the SPRIE process is used to add ordering in the third dimension.

2.2. Colloidal Lithography for 2D Mask Fabrication

We employed NSL to fabricate the etch masks because it allows fast, reliable and large area nanostructuring. **Figure 2**a shows a top FESEM view of a hexagonally packed monolayer array composed of 476 nm diameter colloids. The crystal quality and the orientation were confirmed by the characteristic 6-spot diffraction pattern (Figure 2a, inset). Driving the assembly of particles into geometries other than hexagonal packing (thermodynamically the most stable configuration for spherical objects) was also studied. For instance, we have targeted the realization of a square arrangement that allows the realization of 3D cubic lattice photonic crystals (with complete bandgaps) as detailed below. This was performed by an edge meniscus driven self-assembly technique originally developed by Yuan and co-workers.[36] During the colloidal film elevation with the employed support a considerable amount of water is trapped. While drying, depending on the size of the sample and the compaction degree of the colloidal film, the configuration of the receding contact line of the liquid menisci will influence the colloids' packing configuration. Consequently, in our case, the small size of the silicon chip and the hydrophobicity of the plastic support gave rise to a square-shaped meniscus starting at the edges and going towards the center of the sample. This forced the colloidal assembly into a square arrangement rather than a hexagonal packing (Figure 2b).

Subsequent processing included the colloid size reduction through an O_2 plasma etch and the metallic mask deposition. The anisotropy of the O_2 etch maintained the initial packing configuration and the appropriate profile for metal deposition and lift off (Figure 2c,d). Finally, after the metal lift-off, the samples were solvent cleaned under sonication to remove any polystyrene or metal residuals from the surface. At this stage, the samples consisted in holey metal films on top of the silicon chips that were used subsequently as etch masks (Figure 2e). A high quality mask with uniform hole size distribution can be seen clearly. The mask opening has a major influence on the etched profile due to diffusion constraints and, hence, having a narrow size distribution allows the realization of high quality photonic lattices.

2.3. Direct 3D Structuring of Silicon

The SPRIE protocol was applied to NSL-patterned silicon substrates to build a variety of 3D structures (**Figure 3** and **4**). Under

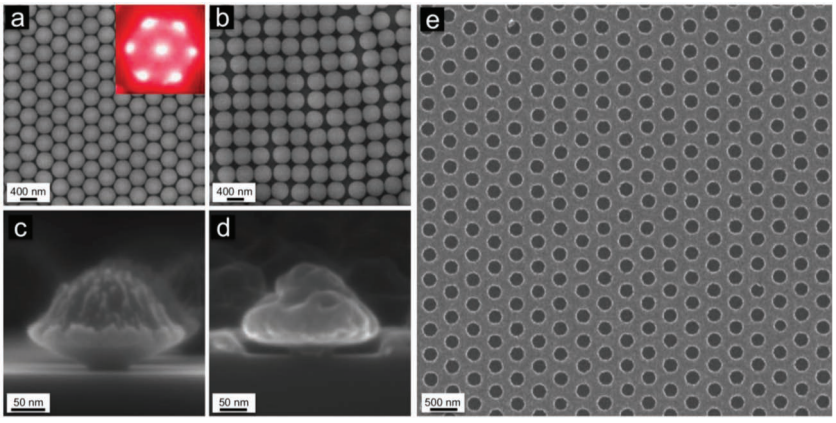

Figure 2. NSL mask fabrication. a) Ordered hexagonal and b) square arrangements realized using 476-nm diameter polystyrene spheres. Inset to (a): the diffraction pattern obtained using a 2-mm diameter laser beam confirming the high quality of the colloidal monolayer film. The monolayer was deposited on glass and the diffraction pattern was projected on a paper sheet. c) Side-view of a colloidal particle after size reduction and d) after Al deposition. e) Characteristic FESEM image after the colloid lift-off evidencing the uniform size distribution of the holes in the metal film mask.

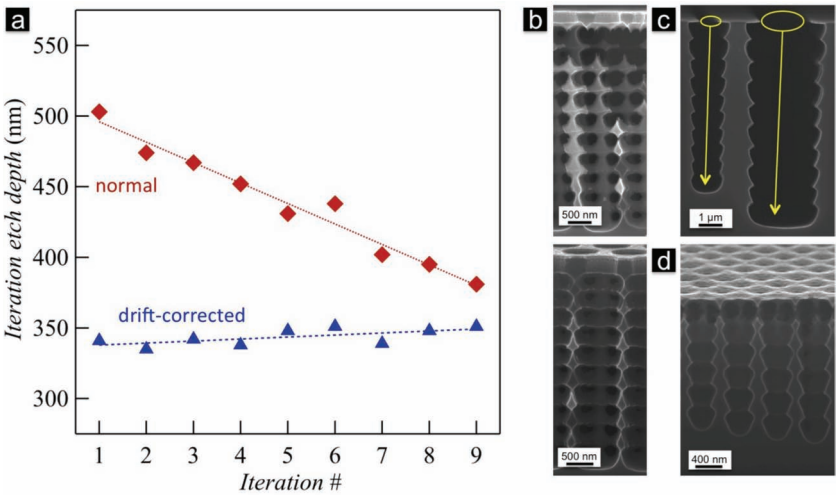

Figure 3. Diffusion-limited SPRIE processing. a) Variation of the etch depth per iteration as a function of the cycle number for the normal and drift-corrected protocols. A 0.5 s increment in the etch time per etch-period was used for the latter. b) FESEM images of the etched profiles for both cases (top: uncorrected, bottom: corrected). c) The influence of mask hole diameter upon the etch depth. d) Even small variations in the mask features, due to the fabrication tolerance, are found to influence the etch depth.

optimized conditions, the number of processing iterations (i.e., pump-purge → etch → passivation) translated into the number of crystal periods along the *z*-direction (normal to the substrate surface). The duration of the fluoropolymer passivation was found to minimally alter the overall processing quality and was kept at 7 to 9 s per iteration. Conversely, the etch duration (per iteration) deeply impacted the etch profile as the process was found to be diffusion limited. For instance, while maintaining a constant etch time (Figure 3a, solid diamonds, $t = 7$ s etch time), a linear decrease in the iteration etch depth was observed. Obviously, this configuration is not appropriate for the realization of photonic crystals where constant periodicity is required. We found that by continuously adapting the etching time, the drift can be corrected. For instance, by implementing a linear time increase for each etch iteration (Figure 3a, solid triangles, $t_0 = 3$ s, $\Delta t = 0.5$ s) a constant lattice parameter of ≈350 nm was realized for more than nine periods. Corresponding FESEM cross-section images are shown in Figure 3b. The crystal quality enhancement is evident and it is clear that for the non-corrected drift structures the top most parts are over-etched leading to fragilization.

The observed behavior can be explained by a diffusion controlled process in high aspect ratio channels with small openings (<500 nm in diameter) during SPRIE processing. The diffusion of the reactants towards the reaction front proceeds only through the mask openings and with the increase in the etch depth, the reactive and reacted species will take more time to diffuse. The passivation reaction generates only few volatile species, explaining possibly why we do not observe any major

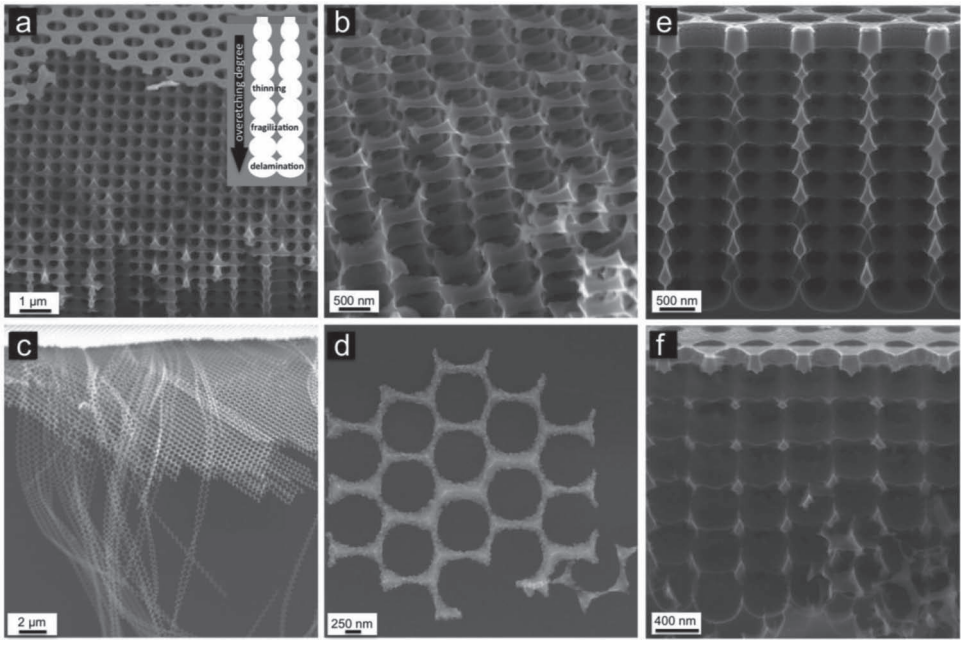

Figure 4. SPRIE designs. a,b) Progressive thinning of the vertical sustaining walls due to extended etching leads to structural fragilization. c,d) By further increasing the etching time, complete delamination is achieved leading to the formation of kinked silicon nanoribbons. Inset to (a): schematics of the structural evolution vs. lateral etch extent in SPRIE. e,f) Proper adjustment of the etch times leads to ordered 3D lattices. FESEM images show examples of the fabricated structures in silicon. Hexagonal (e) and cubic (f) lattices obtained using different colloidal nanosphere arrangements (hexagonal and square, respectively; see Figure 2 for examples of the mask configurations).

influence of the passivation reaction time on the etch profile. The etch reaction however, requires two competing processes: a large volume of reacted species has to be evacuated while, at the same time, fresh reactive species have to be supplied in order to allow the reaction to proceed. Consequently, increasing the aspect ratio of the etched channels will require more time for the respective species to diffuse resulting in a lower etch rate. This corroborates with the data shown in Figure 3a,b. Another consequence of the diffusion-limited nature of the etch process is the influence of the mask feature size on the etch rate. This can be clearly seen in Figure 3c where two channels are etched at different rates due to dissimilar sizes of mask features. Figure 3d shows the same effect at smaller scale. Nominally with the same size, the small variations in the mask size here resulted in lattice dislocations along the *z*-direction. Though detrimental for the photonic crystal quality in the present form, this protocol facet could be optimized and smartly exploited by alternating openings with different sizes in a controllable fashion that will lead to the generation of even more complex 3D lattices.

With drift-corrected etching parameters, we fabricated a large variety of ordered 3D structures (Figure 4). By controlling the lateral extent of the etch step, various configurations have been achieved (inset to Figure 4a). Over-etching gradually resulted in the thinning of the sustaining silicon walls (Figure 4a) leading to progressive fragilization (Figure 4b) up to complete delamination of 1D or 2D silicon stacks (Figure 4c,d). The lateral etch extent can be varied independently for every iteration allowing for the fine-tuning of the material volume fraction, delamination of 3D photonic slabs at predefined iterations and insertion of in-plane defects (see **Figure 5**). By properly combining the 2D mask design with optimized SPRIE parameters (i.e., drift correction and lateral etch extent), high-quality 3D photonic crystals can be obtained. For instance, we have transferred the 2D hexagonal and square colloidal packings (Figure 2a,b) into hexagonal and cubic silicon-based photonic crystals, respectively (Figure 4e,f). The cubic lattice photonic crystal is of a particular interest since the structure shown in Figure 4f might display a complete photonic band gap (see Supporting Information, Figure S1). It is important to note that the SPRIE protocol is insensitive to both mask and depth-scales. For instance, it was optimized to produce high quality 3D lattices using 480 nm and 980 nm diameter colloids. We would like to emphasize the fact that the 2D array to 3D lattice transfer through SPRIE is realized in a simple one-step processing protocol (see Supporting Information, Figure S2 for more large-area 3D structures realized using the single-step SPRIE protocol).

2.4. Defect Engineering

The lateral etching extent can be finely controlled for the entire SPRIE or just for distinct iterations by simply adapting the reaction time. This allows for in-plane defect engineering with precise position and configuration. One example is shown in Figure 5a. The top most part, accomplished in the first 8 iterations, was etched following the same procedure as for the structures shown in Figure 3. The etch time during the 9th iteration was increased to 12 s, compared to 7 s for the 8th cycle, resulting in a more pronounced protrusion. Further increasing the etch time enables delamination of the 3D photonic crystal slab with subsequent possibilities for transfer onto other substrates like flexible polymer sheets. Additional design elements were added by using a dual etch mask (Figure 5b,c). This was attained by combining a standard photolithography-defined plain metal mask (Figure 5b) with a NSL defined etch mask deposited on top (Figure 5c). Here, the NLS mask is used to realize the in-plane structuring, while the photolithography-defined mask confines the photonic crystal region. Confinement resolution down to a single unit cell is possible by using deep-UV or electron beam lithography. Overlay alignment of the two masks was easily achieved. By analyzing the laser beam diffraction pattern, the crystalline orientation of the NSL layer was first identified (see Figure 2a). The accurate deposition of the respective film on top of the photolithography-defined patterns completes the process of overlay alignment (Figure 5c). Finally, both types of defect engineering, in-plane size modulation and dual-mask confined etching, could be elegantly combined to reach more complex functionalities and 3D photonic architectures through SPRIE.

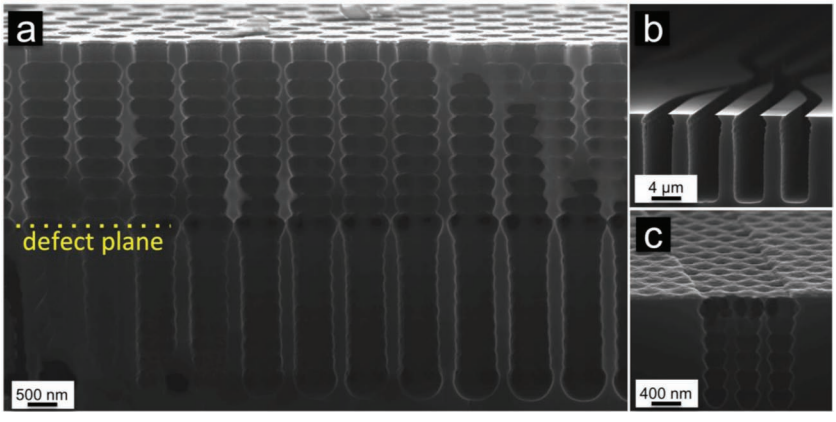

Figure 5. Defect engineering. a) Defect plane induced by increasing the etching time at the 9th iteration. A further increase in the etch time will result in the delamination of the 3D crystal slab. b) Etched profile using a photolithography-defined etch mask displaying micrometer patterns. c) Close-up view of the crystal slab obtained via dual mask etching where a colloidal mask is used in combination with a standard photolithography mask.

2.5. Photonic Crystal Structuring

By adequately matching the lattice parameters of the 2D colloid array (defined by the nominal sphere size and packing configuration) with the *z*-period, high quality 3D photonic crystal lattices were fabricated. The calculated and measured optical properties for a representative 3D photonic crystal, measured using an objective with a numerical aperture (NA) of 0.58 for focusing and collection are shown in **Figure 6**a. A pronounced feature at 2.27 µm is clearly observed in both transmittance and reflectance spectra. We attribute the slight disagreement between the theoretical and the experimental spectra to details

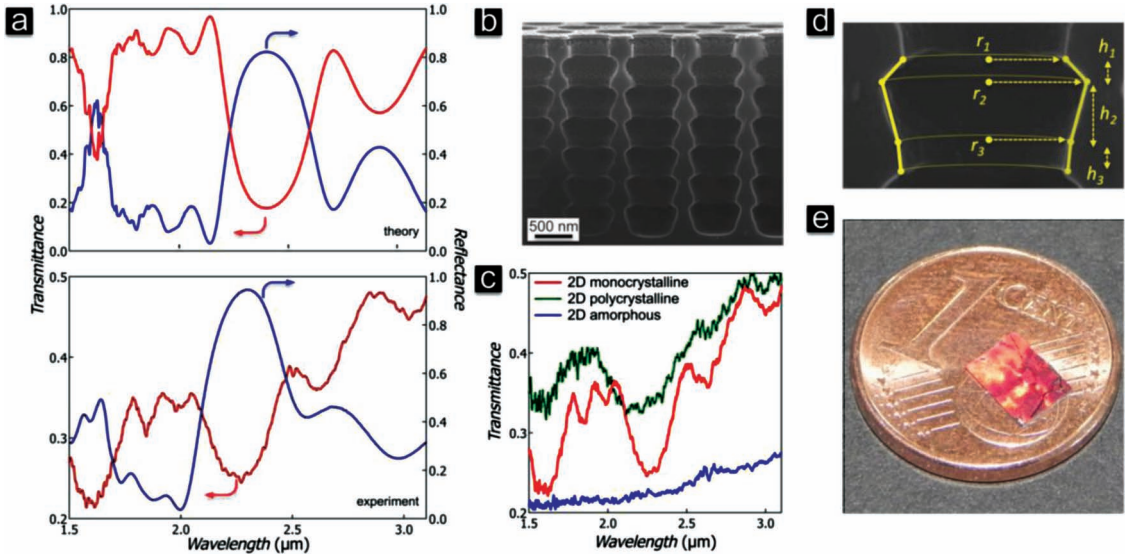

Figure 6. Optical performance. a) Calculated and measured transmittance spectra taken under normal incidence for a representative 3D photonic crystal obtained using SPRIE. b) FESEM cross-section view of the analyzed structure. c) The characteristic features at 1.60 μm and 2.27 μm (red line) are less pronounced or vanish when scanning polycrystalline (green line) and amorphous areas (blue line), respectively (see main text and Supporting Information for details). d) Structural details of the unit cell used for the computation. e) Optical photograph of the sample shown in panel (b) after cleaving.

of the pore and the lattice that are not replicated by the model that our calculations are based on (see Experimental Section and Figure 6d). In order to make sure that the detected dip in the transmission spectra is not only due to the periodicity in the *z*-direction defined by the etch-modulation, we have probed several areas on the sample with different pore arrangements, i.e., areas of the sample in which differently ordered etch-masks were present (see Supporting Information Figure S2a for an example of a large area monocrystalline sample and Figure S3 for measurement and interpretation details of areas with distinct 2D orderings of the etch apertures). Regions in which monocrystalline, polycrystalline, and disordered (amorphous) 2D masks were present have been examined. Clearly, the intensity of the transmission dip diminishes when moving from mono- to polycrystalline areas whereas it vanishes on amorphous regions. Since the amorphous and polycrystalline regions have the same *z*-periodicity as the monocrystalline regions, we can exclude the hypothesis that the observed feature in the transmission spectra is simply due to the *z*-periodic modulation of the material filling fraction induced by SPRIE. Hence, we attribute the photonic signature to the ordered 3D structure of the crystal.

3. Conclusions

In conclusion, we present SPRIE, a simple and robust protocol for direct structuring of silicon-based 3D photonic crystals. Through a single processing step, SPRIE transcribes 2D colloidal crystal arrangements into well-ordered 3D architectures. This is achieved by fine tuning of the plasma chemistry balance. The lateral etch extent controls a large variety of 3D topologies, useful in the delamination of 3D photonic crystals slabs or for the controlled insertion of structural defects. While dual-type masking creates opportunities for confining the 3D photonic slab structuring area, further functionalities and the implementation of complete 3D photonic bandgaps could be enabled by exploring the colloidal mask symmetries or by applying angled-etching. With proper adjustment of the lattice parameters, high quality Si photonic crystals with distinct optical characteristics were obtained. The presented technique paves the way for large-area fabrication of photonic architectures through simple and reliable protocols.

4. Experimental Section

Experiment: Aqueous suspensions of polystyrene colloidal particles (Microparticles GmbH) with different nominal sizes (0.48 μm and 0.92 μm) were used as received. Silicon substrates ([100], *p*-type *B* doped, 10–15 Ω.cm, 200 μm thick, double side polished) have been used as fabrication platforms. Prior to the NSL, the 1 × 1 cm^2 silicon square substrates have been soaked in a freshly prepared H_2SO_4/H_2O_2 solution to clean and render the silicon surface hydrophilic. For square lattice assemblies, smaller silicon chips (0.4 × 0.4 cm^2) were attached to a hydrophobic plastic film before the colloidal film uptake. The 2D colloidal self-assembly was performed using already documented protocols.[37] Briefly, the colloidal suspension was first diluted with ethanol (typically 1 to 4–8 volume ratio) to improve the buoyancy of the particles. To neutralize the negatively charged sulfate groups and render hydrophobic the surface of the particles, small amounts of sulfuric acid or styrene were added (less than 0.1%). The prepared suspension was then gently dispersed on the surface of water in a Petri dish. Progressive appearance of a colloidal polycrystalline monolayer at the water surface could be visualized by a mixture of iridescent colors. Subsequent recrystallization and consolidation through the addition of minute amounts of TX100 surfactant enabled the fabrication of centimeter scale colloidal monocrystalline domains at the water surface. The colloidal films were subsequently lifted up using pre-cleaned silicon substrates and dried in air.

The size of the polystyrene particles was reduced via a reactive ion etching step using O_2 plasma chemistry (Plasma Therm Batchtop RIE m/91, 10 sccm O_2 flow, 25 W RF power, 250 mTorr, etch rate ≈150 nm/min). Hard etch masks were made by physical vapor deposition

of aluminum (50 nm thick, 99.99% purity, Goodfellow). The lift-off was performed using adhesive tape. A short O_2 plasma exposure was performed in order to remove polystyrene residuals left on the surface of the silicon. SPRIE of silicon was performed using an inductively coupled plasma system (STS ICP). The operational parameters for the etch and passivation steps were: 130 sccm SF_6/13 sccm O_2 gas flow rate, 10 W RF/600 W ICP power, 26 mTorr; and 85 sccm C_4F_8 gas flow rate, 0 W RF/800 W ICP power, 11 mTorr, respectively. While the passivation time (typically 7 to 9 s) was found to have a minimal influence on the etch uniformity, the etch time had to be adjusted depending on the targeted structure and the size of the mask opening. Additionally, a pump–N_2 purge step (10 to 30 s duration) was performed after each passivation/etch iteration (see Section 2 for details). For optical characterization, the Al mask layer was removed by dipping the sample in a diluted (5 wt%) HNO_3 solution.

The structural characterization was performed using a Zeiss Supra 60VP field emission scanning electron microscope (FESEM). Optical characterization (transmission and reflectance spectroscopy) was carried out using an FTIR-Spectrometer (Thermo Nicolet Nexus 870 Infrared Microscope) using an Infinity Reflachromat objective (15× ∞, NA = 0.58). Non-structured areas on the samples served as a reference for the transmission measurements, while an aluminum coated silicon chip served as a reference for the reflectance measurements. A 60 µm × 60 µm area was selected for measurement by placing an aperture into the beam path.

Numerical Modeling: The optical properties of the structure under investigation were simulated using the Fourier modal method (FMM, also known as scattering-matrix technique), a standard tool for the characterization of photonic crystals and metamaterials.[38] All used parameters were deduced from electron microscope images (for example, Figure 6d). The hexagonal (primitive) unit cell with lattice constant a = 920 nm and height $h = 0.5052 \cdot a$ consists of a background silicon matrix ($\varepsilon_{bg} = 11.8336$) and three embedded stacked frustums of air ($\varepsilon_{frustum} = 1.0$) as schematically depicted in Figure 6d ($r_1 = 0.337a$, $r_2 = 0.449a$, $r_3 = 0.3530a$, $h_1 = 0.143a$, $h_2 = 0.241a$, $h_3 = 0.121a$). It was discretized in the transversal plane by 1024 × 1024 sampling points and by 20 layers of equal thickness in the main propagation direction (along the frustum's axes). The whole simulated structure consists of six unit cells stacked on top of a semi infinite silicon half space and covered with an additional perforated silicon layer ($h_{cover} = 0.281a$, $r_{cover} = r_1$). As light source we set up a plane wave under different angles of incidence to mimic the NA of the experimental setup and calculated the total transmittance and reflectance into all diffraction orders. The simulations were performed using a basis set of 295 plane waves for the modal expansion. The resulting transmittance and reflectance spectra for azimuth angles ϕ = 0°, 30° (with respect to the lattice vectors) and polar angles θ = 0°, 5°, 10°, 15°, 20°, 25°, 30° and 35° (with respect to surface normal) have been arithmetically averaged.

Supporting Information

Supporting Information is available from the Wiley Online Library or from the author.

Acknowledgements

A. V., A. F., and T. Z. contributed equally to this work. A.V. acknowledges F.R.S.-FNRS and MC2ACCESS—Program, Contract No. 026029, as part of "Access to Research Infrastructures", FP6 for the financial support. The work in Louvain-la-Neuve, Belgium, was supported by the TINTIN project–ARC, Communauté Française de Belgique, and the Belgian National Fund for Scientific Research (F.R.S. - FNRS) via the FRFC projects 2.4505.09 and 2.4510.11. The Karlsruhe research was supported by subprojects A1.2 and A1.4 of the DFG-Center for Functional Nanostructures (CFN). T.Z. acknowledges financial support by the Carl-Zeiss-Foundation. The Ph.D. education of A.F. and T.Z. is embedded into the Karlsruhe School of Optics & Photonics.

Received: April 24, 2012
Revised: August 22, 2012
Published online: October 8, 2012

[1] S. Kim, S. Lee, S. Yang, G.-R. Yi, *NPG Asia Mater.* **2011**, *3*, 25–33.
[2] J. F. Galisteo López, M. Ibisate, R. Sapienza, L. S. Froufe Pérez, Á. Blanco, C. Lopez, *Adv. Mater.* **2011**, *23*, 30–69.
[3] A.-P. Hynninen, J. H. J. Thijssen, E. C. M. Vermolen, M. Dijkstra, A. Van Blaaderen, *Nat. Mater.* **2007**, *6*, 202–205.
[4] C. M. Soukoulis, M. Wegener, *Nat. Photonics* **2011**, *5*, 523–530.
[5] A. Arico, P. Bruce, B. Scrosati, J. Tarascon, W. Van Schalkwijk, *Nat. Mater.* **2005**, *4*, 366–377.
[6] G. Konstantatos, E. H. Sargent, *Nat. Nanotechnol.* **2010**, *5*, 391–400.
[7] J. D. Joannopoulos, S. G. Johnson, J. N. Winn, R. D. Meade, *Photonic Crystals: Molding the Flow of Light (2nd Ed.)*, Princeton University Press, Princeton, NJ **2008**.
[8] J. A. Schuller, E. S. Barnard, W. Cai, Y. C. Jun, J. S. White, M. L. Brongersma, *Nat. Mater.* **2010**, *9*, 193–204.
[9] F. Marlow, Muldarisnur, P. Sharifi, R. Brinkmann, C. Mendive, *Angew. Chem. Int. Ed.* **2009**, *48*, 6212–6233.
[10] A. Stein, F. Li, N. R. Denny, *Chem. Mater.* **2008**, *20*, 649–666.
[11] A. Diacon, E. Rusen, A. Mocanu, P. Hudhomme, C. Cincu, *Langmuir* **2011**, *27*, 7464–7470.
[12] T. Ding, K. Song, K. Clays, C.-H. Tung, *Langmuir* **2010**, *26*, 11544–11549.
[13] I. D. Hosein, S. H. Lee, C. M. Liddell, *Adv. Funct. Mater.* **2010**, *20*, 3085–3091.
[14] S. A. Rinne, F. García-Santamaría, P. V. Braun, *Nat. Photonics* **2008**, *2*, 52–56.
[15] F. J. Aparicio, G. Lozano, I. Blaszczyk-Lezak, A. Barranco, H. Miguez, *Chem. Mater.* **2009**, *22*, 379–385.
[16] M. Qi, E. Lidorikis, P. Rakich, S. Johnson, J. Joannopoulos, E. Ippen, H. Smith, *Nature* **2004**, *429*, 538–542.
[17] M. Deubel, G. Von Freymann, M. Wegener, S. Pereira, K. Busch, C. M. Soukoulis, *Nat. Mater.* **2004**, *3*, 444–447.
[18] G. Von Freymann, A. Ledermann, M. Thiel, I. Staude, S. Essig, K. Busch, M. Wegener, *Adv. Funct. Mater.* **2010**, *20*, 1038–1052.
[19] M. Campbell, D. Sharp, M. Harrison, R. Denning, A. Turberfield, *Nature* **2000**, *404*, 53–56.
[20] S. Jeon, J. U. Park, R. Cirelli, S. Yang, C. E. Heitzman, P. V. Braun, P. J. A. Kenis, J. A. Rogers, *Proc. Natl. Acad. Sci. USA* **2004**, *101*, 12428–12433.
[21] C. H. Chang, L. Tian, W. R. Hesse, H. Gao, H. J. Choi, J. G. Kim, M. Siddiqui, G. Barbastathis, *Nano Lett.* **2011**, *11*, 2533–2537.
[22] A. Vlad, C. A. Dutu, P. Guillet, P. Jedrasik, C.-A. Fustin, U. Södervall, J.-F. Gohy, S. Melinte, *Nano Lett.* **2009**, *9*, 2838–2843.
[23] I. Staude, G. Von Freymann, S. Essig, K. Busch, M. Wegener, *Opt. Lett.* **2011**, *36*, 67–69.
[24] S. Wong, M. Deubel, F. Pérez-Willard, S. John, G. A. Ozin, M. Wegener, G. Von Freymann, *Adv. Mater.* **2006**, *18*, 265–269.
[25] J. Schilling, F. Muller, S. Matthias, R. Wehrspohn, U. Gosele, K. Busch, *Appl. Phys. Lett.* **2001**, *78*, 1180–1182.
[26] S. Takahashi, K. Suzuki, M. Okano, M. Imada, T. Nakamori, Y. Ota, K. I. Susumu, S. Noda, *Nat. Mater.* **2009**, *8*, 721–725.
[27] J. van den Broek, L. Woldering, R. Tjerkstra, F. Segerink, I. Setija, W. Vos, *Adv. Funct. Mater.* **2012**, *22*, 25–31.
[28] J. Zhang, Y. Li, X. Zhang, B. Yang, *Adv. Mater.* **2010**, *22*, 4249–4269.
[29] S. Y. Lee, L. Gradon, S. Janeczko, F. Iskandar, K. Okuyama, *ACS Nano* **2010**, *4*, 4717–4724.

[30] A. Vlad, I. Huynen, S. Melinte, *Nanotechnology* **2012**, *23*, 285708.
[31] Y. Vlasov, X. Bo, J. Sturm, D. Norris, *Nature* **2001**, *414*, 289–293.
[32] M. R. Jones, K. D. Osberg, R. J. Macfarlane, M. R. Langille, C. A. Mirkin, *Chem. Rev.* **2011**, *111*, 3736–3827.
[33] S. Venkataraman, G. J. Schneider, J. Murakowski, S. Shi, D. W. Prather, *Appl. Phys. Lett.* **2004**, *85*, 2125–2127.
[34] F. Laermer, A. Schilp, *U.S. Patent No. 5501893* **1996**.
[35] B. Wu, A. Kumar, S. Pamarthy, *J. Appl. Phys.* **2010**, *108*, 051101.
[36] T. Zhang, J. Qian, X. Tuo, J. Yuan, *Langmuir* **2010**, *26*, 3690–3694.
[37] A. Kosiorek, W. Kandulski, P. Chudzinski, K. Kempa, M. Giersig, *Nano Lett.* **2004**, *4*, 1359–1363.
[38] K. Busch, G. Von Freymann, S. Linden, S. F. Mingaleev, L. Tkeshelashvili, M. Wegener, *Phys. Rep.* **2007**, *444*, 101–202.